J. Fluid Mech. (2020), *vol.* 884, A26. © Cambridge University Press 2019
doi:10.1017/jfm.2019.840

Large-scale structures in high-Reynolds-number rotating Waleffe flow

Shafqat Farooq[1], **Martin Huarte-Espinosa**[2] **and Rodolfo Ostilla-Mónico**[1,†]

[1]Cullen College of Engineering, University of Houston, Houston, TX 77204, USA

[2]University of Houston's Hewlett Packard Enterprise Data Science Institute, University of Houston, Houston, TX 77204, USA

(Received 25 March 2019; revised 7 August 2019; accepted 1 October 2019)

We perform direct numerical simulations of rotating turbulent Waleffe flow, the flow between two parallel plates with a sinusoidal streamwise shear driving force, to study the formation of large-scale structures and the mechanisms for momentum transport. We simulate different cyclonic and anticyclonic rotations in the range of dimensionless rotation numbers (inverse Rossby numbers) $R_\Omega \in [-0.16, 2.21]$, and fix the Reynolds number to $Re = 3.16 \times 10^3$, large enough such that the shear transport is almost entirely due to Reynolds stresses and viscous transport is negligible. We find an optimum rotation in the anticyclonic regime at $R_\Omega = 0.63$, where a given streamwise momentum transport in the wall-normal direction is achieved with minimum mean energy of the streamwise flow. We link this optimal transport to the strength of large-scale structures, as was done in plane Couette flow by Brauckmann & Eckhardt (*J. Fluid Mech.*, vol. 815, 2017, pp. 149–168). Furthermore, we explore the large-scale structures and their behaviour under spanwise rotation, and find disorganized large structures at $R_\Omega = 0$ but highly organized structures in the anticyclonic regime, similar to the rolls in rotating plane Couette and turbulent Taylor–Couette flow. We compare the large-scale structures of plane Couette flow and Waleffe flow, and observe that the streamwise vorticity is localized inside the cores of the rolls. We show that the rolls take energy from the mean flow at long time scales, and relate these structures to eigenvalues of the streamfunction.

Key words: turbulent convection, turbulent boundary layers, Taylor–Couette flow

1. Introduction

While turbulent flows are generally chaotic and random, coherent large-scale motions can exist within them. Wall-bounded turbulent flows are not an exception, and large-scale organized structures have been reported in both experiments and numerics (Jimenez 2012). The study of structures was pioneered in channel flow, i.e. the pressure-driven flow between two parallel plates, a popular model to study wall-bounded turbulence. Using large-eddy simulation, Moin & Kim (1982) found large-amplitude streamwise vortical structures concentrated near the wall. These large-scale structures were attributed to a splatting effect (a net transfer of energy

† Email address for correspondence: rostilla@central.uh.edu

between perpendicular velocity fluctuations) and to Helmholtz-type instabilities of intense shear layers at and near the wall. Similar large-scale structures were also found by Moser & Moin (1984) using direct numerical simulation (DNS) in turbulent channel flow with a curved geometry, and by Kim, Moin & Moser (1987) in a fully turbulent channel. Kim *et al.* (1987) further characterized these structures through local maxima and minima of the streamwise vorticity, i.e. a streamwise vortex model. With the increased availability of computational power, the achievable Reynolds numbers and domain sizes in simulations have kept on growing. Large coherent structures have still been observed even for the recent simulations at $Re_\tau \approx 5200$ by Lee & Moser (2015). Coherent flow structures have also been observed in other types of high-Reynolds-number wall-bounded flows, including pipe flows (Eckhardt *et al.* 2007), plane Couette flow, i.e. the shear flow between two parallel plates, in turbulent boundary layers (Smits, McKeon & Marusic 2011), and in von Kármán flow, i.e. the flow between two coaxial rotating discs (Zandbergen & Dijkstra 1987; Ravelet *et al.* 2004).

Taylor–Couette flow (Grossmann, Lohse & Sun 2016), the flow between two coaxial and independently rotating cylinders, is another canonical wall-bounded flow where coherent large-scale structures are present. Their formation has usually been attributed to centrifugal (linear) instabilities since the seminal study by Taylor (1923). Because of this, they are usually referred to as Taylor rolls. Owing to the centrifugal effects, Taylor–Couette flow and its structures have usually been studied from the point of view of angular momentum convection, and not from the perspective of a wall-bounded flow (Lathrop, Fineberg & Swinney 1992). A notable difference between Taylor rolls and more general structures in wall-bounded flows is that Taylor rolls are pinned, i.e. they do not move around the fluid domain, and this is true with increasing Reynolds numbers up to the so-called turbulent Taylor rolls seen at $Re \simeq 10^6$ by Huisman *et al.* (2014). Turbulent Taylor rolls survive at high Reynolds number only for some combinations of curvature and mild outer-cylinder rotation (Huisman *et al.* 2014; Ostilla-Mónico *et al.* 2014). Remarkably, in a Taylor–Couette geometry with a large curvature, rolls do not exist at high Reynolds number for pure inner-cylinder rotation (Ostilla-Mónico *et al.* 2014). This means that something else aside from centrifugal effects must play a role. Numerical studies of Taylor–Couette flow conducted by Sacco, Verzicco & Ostilla-Mónico (2019) found that turbulent Taylor rolls appeared with a combination of shear and mild anticyclonic rotation. Their onset was not controlled by the curvature of the system. At high Reynolds numbers, Taylor rolls would unpin, or even disappear, if anticyclonic rotation was removed. Sacco *et al.* (2019) also found that the rolls are persistent in the limit of vanishing curvature, i.e. when Taylor–Couette flow becomes rotating plane Couette flow, if anticyclonic rotation is present.

This showed that the study of turbulent Taylor rolls could be better approached from a shear flow perspective, and not simply by thinking of them as a continuation of the centrifugal linear instability seen at low Reynolds numbers. Indeed, low-curvature Taylor–Couette flow shows some characteristics of shear flows for Reynolds numbers just beyond the onset of the linear, centrifugal instability. Taylor rolls develop a streamwise modulation, after which they are usually denoted ‘wavy’ Taylor vortices Andereck, Liu & Swinney (1986). This is linked to the appearance of large-scale streaks (Dessup *et al.* 2018). Taylor rolls are then fed by the nonlinear interaction of streaks. This nonlinear interaction between the pinned Taylor roll and the streak was attributed to the activation of the self-sustained process (SSP) of shear flows (Dessup *et al.* 2018), which is described below. In this spirit, Sacco *et al.* (2019) showed that

the energy of turbulent Taylor rolls and streaks varied periodically with a distinct phase shift, and a long-time-scale multistage process energized the pinned structures. But despite the low-Reynolds-number link (Dessup *et al.* 2018), it is not clear how the high-Reynolds-number turbulent Taylor roll–streak process is related to the SSP responsible for the generation of turbulence in shear flows.

The name SSP commonly refers to a multistage process responsible for regenerating wall-bounded turbulence, where streamwise rolls interact with streamwise velocity to cause streaks. These unstable streaks interact nonlinearly, reinforcing the rolls and completing the SSP cycle. Waleffe (1997) was the first to show that a generic process was responsible for the regeneration of turbulence in wall-bounded flows. Unlike earlier studies of the regeneration mechanisms in channel flow (Hamilton, Kim & Waleffe 1995), Waleffe (1997) studied the SSP in a fluid system where the flow is bounded by two infinite stress-free plates and forced using a body shear force. Waleffe (1997) was the first to study this system in detail to assess the role of the no-slip condition in the SSP, even if it had been used by Tollmien (1936) to show that an inflection point was not a sufficient condition for linear instability (Drazin & Reid 2004). Because of this, it has been recently associated with Waleffe's name (Beaume *et al.* 2015; Chantry, Tuckerman & Barkley 2016), and we will refer to it as Waleffe flow from here on.

In the spirit of Waleffe (1997), we set out to investigate whether the large-scale coherent structures of plane Couette and Taylor–Couette flow are part of a more general class of structures, which require only shear (and anticyclonic rotation), as the SSP does, or if they are something distinct, separated from the SSP because they require the presence of a no-slip wall. The natural system to investigate this is rotating Waleffe flow.

The absence of a no-slip wall also provides for a second avenue of investigation. In Taylor–Couette and in rotating plane Couette flow, the transport of torque or shear is greatly enhanced by the presence of large-scale structures. In particular, in Taylor–Couette flow, the angular velocity current, non-dimensionalized as a Nusselt number (Nu_ω), depends mainly on three parameters: first, the shear, which can be non-dimensionalized as a shear Reynolds number, $Re_s = U(r_o - r_i)/\nu$; second, the solid-body system rotation, which appears in the equations as a Coriolis force, and its magnitude can be expressed non-dimensionally as a rotation number, $R_\Omega = 2\Omega(r_o - r_i)/U$; and finally, the curvature, expressed as a radius ratio, $\eta = r_i/r_o$. Here, r_i (r_o) is the inner (outer) cylinder radius, U is a characteristic shear velocity, ν is the kinematic viscosity of the fluid and Ω is the background rotation. Each of these parameters is linked both to the torque and to the presence of large-scale structures (van Gils *et al.* 2012; Brauckmann & Eckhardt 2013; Ostilla-Mónico *et al.* 2014). In the low-curvature regime ($\eta \geqslant 0.9$), where centrifugal forces are negligible, Brauckmann, Salewski & Eckhardt (2016) showed that, at $Re_s \sim O(10^4)$, there are two local maxima in the $Nu_\omega(R_\Omega)$ curve: one narrow and one broad. The 'broad maximum' at $R_\Omega \approx 0.2$ dominated at lower shear Reynolds number (Re_s) and was related to the enhancement of large-scale vortical flow structures (Brauckmann *et al.* 2016). On the other hand, the 'narrow peak' at $R_\Omega = 0.02$ was linked to a shear instability due to turbulent boundary layers (Brauckmann & Eckhardt 2017) and emerged with increasing Re_s. It was argued that this narrow peak would supersede the broad peak at very high Re_s (Brauckmann *et al.* 2016; Brauckmann & Eckhardt 2017), and this was confirmed experimentally (R. Ezeta, unpublished observations).

The broad and narrow peaks in the shear/torque transport were found to exist even in the limit of rotating plane Couette flow, when curvature was completely absent.

If large-scale vortical structures similar to the so-called turbulent Taylor rolls appear in Waleffe flow, one could expect that, in the regions of parameter space where they are strengthened, a similar shear transport enhancement will exist. And if it existed, this optimal transport would survive well into the turbulent regime, as it would not be superseded by boundary layer instabilities from a no-slip wall. Thus the second and third questions we set out to answer are these: (i) Does optimal transport exist in rotating Waleffe flow? (ii) If so, how is it linked to large-scale structure enhancement?

The paper is organized as follows. In § 2, we define the numerical set-up, control parameters, spatial resolution and domain size study. These include details of the numerical scheme (§ 2.1), energy spectrum studies to assess the spatial resolution (§ 2.2) and autocorrelation studies (§ 2.3) to assess the size of the domain. We then detail the results of our investigation in § 3, including a characterization of the transport of shear in § 3.1, the effect of rotation on the statistics of Waleffe flow at high Reynolds number in § 3.2, including a discussion of optimal transport, the effect of rotation on the large-scale structures, and how it is further linked to optimal transport and measures against plane Couette flow in § 3.3, and a further characterization of these structures in § 3.4. We conclude in § 4 with a brief summary and an outline for further research.

2. Numerical set-up

2.1. *Problem set-up and non-dimensionalization*

We perform DNS of rotating Waleffe flow in a three-dimensional domain that is bounded by free-slip walls in the y direction at $y = 0$ and $y = d$, and is periodic in the streamwise (x) and spanwise (z) directions with periodicity lengths L_x and L_z, respectively. A body force $\boldsymbol{f}$ is used to force the flow. A Coriolis body force is used to simulate solid-body rotation in the flow, which can be either cyclonic, i.e. where the spanwise rotation vector is parallel to the vorticity of the laminar base flow ($R_\Omega < 0$), or anticyclonic, i.e. the spanwise rotation vector is antiparallel to the vorticity of laminar base flow ($R_\Omega > 0$). With this, the Navier–Stokes equations thus read

$$\frac{\partial \boldsymbol{u}}{\partial t} + \boldsymbol{u}\cdot\boldsymbol{\nabla}\boldsymbol{u} + 2\Omega(\boldsymbol{e}_z \times \boldsymbol{u}) = -\boldsymbol{\nabla} p + \nu\nabla^2\boldsymbol{u} + \boldsymbol{f}, \tag{2.1}$$

which are solved alongside the incompressibility condition

$$\boldsymbol{\nabla}\cdot\boldsymbol{u} = 0, \tag{2.2}$$

where $\boldsymbol{u}$ is the velocity, Ω is the background spanwise rotation, p is the pressure and t is time.

The geometrical configuration and the input body force of Waleffe flow is show in figure 1. The velocities in the x, y and z directions are denoted by u, v and w, respectively. A streamwise shear body force is required to force the flow, as, unlike plane Couette, flow no energy is injected through the walls. A sinusoidal profile is chosen, i.e. $\boldsymbol{f} = F\cos(\beta y)\boldsymbol{e}_x$, with $\beta = \pi/d$, analogous to the set-up used in Waleffe (1997). This means that the force is maximum, but in opposite directions at both slip walls, and zero at the mid-plane. The force must have zero average as otherwise the flow would constantly accelerate unopposed by the free-slip walls.

Furthermore, in the absence of the Dirichlet (no-slip) boundary condition, the system is completely Galilean-invariant. An arbitrary translation velocity can be added in either the streamwise or spanwise direction with no effect. A reference

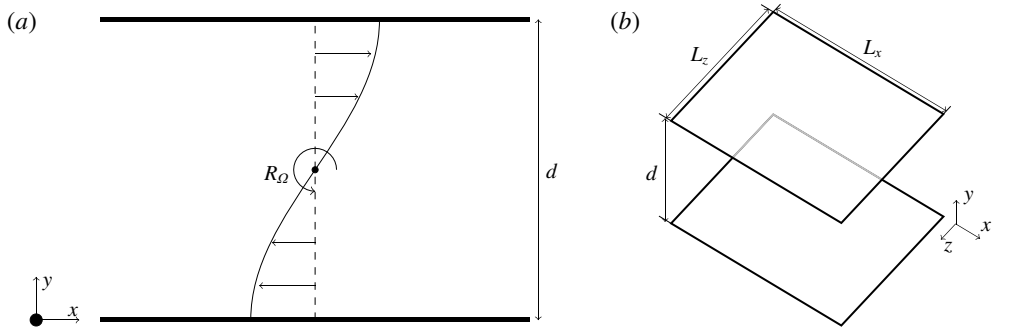

FIGURE 1. (*a*) Two-dimensional spanwise cut of the system showing the streamwise shear force and background rotation of the Waleffe flow system. The y origin of the system is shown as a thick black circle. (*b*) Three-dimensional view of the simulation geometry.

frame must be chosen, and we take the one for which the mean streamwise and spanwise velocities are zero. We will denote with the operator $\langle\cdots\rangle$ a streamwise, spanwise and temporal average. In this spirit, $\langle\phi\rangle$ represents a mean quantity, ϕ' the instantaneous fluctuation around the mean quantity, and $\langle\phi'\rangle$ the root-mean-square fluctuation around this mean.

The equations are non-dimensionalized using the distance between the walls d and the forcing amplitude F. We define a characteristic velocity $\tilde{U}$ for non-dimensionalization as $\tilde{U} = \sqrt{Fd}$. We note that we use a different characteristic velocity than the one classically used for Waleffe flow (cf. Beaume *et al.* 2015), as we focus on the fully turbulent case, and not in perturbations around the laminar state. This definition results in a Reynolds number defined as $Re = \tilde{U}d/\nu = \sqrt{Fd^3}/\nu$, which is our first control parameter. The second non-dimensional control parameter accounts for the cyclonic and anticyclonic rotation of the system, and is defined as $R_\Omega = 2\Omega d/\tilde{U} = 2\Omega d/\sqrt{Fd}$. For this study, we fix $Re = 3.16 \times 10^3$, large enough such that the flow is fully turbulent and that the shear transport takes place purely through Reynolds stresses (cf. § 3.1), and vary R_Ω in the range $[-0.16, 2.21]$ to study the effect of rotation. After the initial transient, we run the simulations between 200 and 250 $d/\tilde{U}$ time units to collect statistics.

The equations are discretized in space using a second-order energy-conserving centred finite difference scheme, while temporal discretization is done using a third-order Runge–Kutta method for the explicit terms and a second-order Adams–Bashforth scheme for the implicit viscous terms in the wall-normal direction. The simulation code used is based on the highly parallel FORTRAN-based AFiD (www.afid.eu), which has been used mainly for simulating turbulent Rayleigh–Bénard convection and Taylor–Couette flow (van der Poel *et al.* 2015). This code has been comprehensively validated. Detailed information regarding the code algorithms can be found in Verzicco & Orlandi (1996) and van der Poel *et al.* (2015).

2.2. *Resolution study*

For determining what is an adequate spatial resolution of the flow, a series of simulations were performed at $Re = 3.16 \times 10^3$, for both no rotation ($R_\Omega = 0$) and mild anticyclonic rotation ($R_\Omega = 0.32$). We can expect the wall-normal resolution to be less stringent in Waleffe flow due to the absence of the no-slip boundary condition.

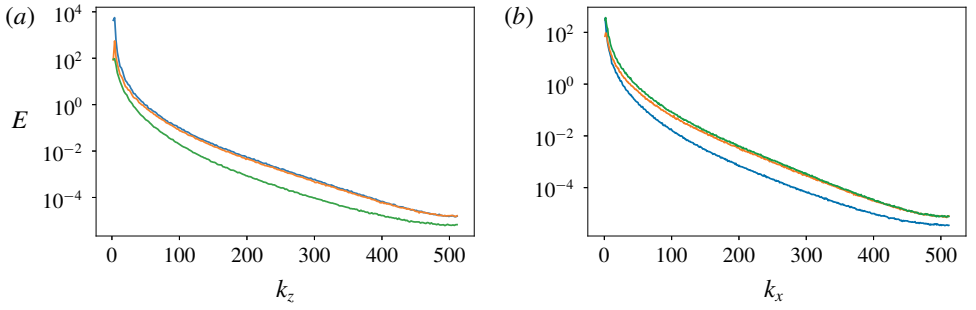

FIGURE 2. Energy spectra for the streamwise velocity u (blue), the wall-normal velocity v (orange) and the spanwise velocity w (green) in the spanwise (a) and streamwise (b) directions at the mid-gap at $R_\Omega = 0$.

However, the streamwise and spanwise directions were found to be more restrictive than a plane Couette flow simulation at comparable Reynolds numbers. Indeed, if one compares the Kolmogorov length scale η_K at $Re \sim 3 \times 10^3$ for both systems, we obtain that η_K is between five and six times smaller for non-rotating Waleffe flow than for non-rotating plane Couette flow.

Adequate resolution for the streamwise and spanwise directions was ensured through a spectral analysis of velocity data. We found that for $L_x/d = 2\pi$ and $L_z/d = \pi$, $N_x = 1024$ and $N_z = 512$ points distributed uniformly were enough to accurately represent the velocity spectra at mid-gap at both no rotation and $R_\Omega = 0.32$. An extended dissipative regime at high wavenumbers, with energy $E \sim \exp(-k)$, is seen in figure 2 for both the streamwise and the spanwise directions.

We note that both homogeneous directions have the same effective grid spacing, $\Delta/d = 6.13 \times 10^{-3}$. Non-dimensionalized by the Kolmogorov length scale, this is approximately $\Delta/\eta_K \approx 2.51$. Using this grid spacing in the wall-normal direction would result in a grid of $N_y \approx 163$ points. For safety, we use $N_y = 384$, and cluster points near the wall, such that the minimum wall-normal grid spacing is $\Delta/d = 3.84 \times 10^{-4}$ and the maximum wall-normal grid spacing is $\Delta/d = 3.85 \times 10^{-3}$, or $0.157 \lesssim \Delta/\eta_K \lesssim 1.58$ in Kolmogorov units.

2.3. *Domain periodicity study*

We performed a domain-size study in order to quantify the effect of the spanwise and streamwise periodicity lengths on the flow field statistics and on the large structures that might be present in the flow. We simulated several domain sizes, where L_x and L_z were doubled each time to produce larger and larger domains. The spatial resolution in both x and z directions was also doubled every time the domain was doubled, to keep the resolution from the previous section. We refer to the domains henceforth as 'very small' ($L_x/d = \pi$ and $L_z/d = \pi/2$), 'small' ($L_x/d = 2\pi$ and $L_z/d = \pi$), 'medium' ($L_x/d = 4\pi$ and $L_z/d = 2\pi$) and 'large' ($L_x/d = 8\pi$ and $L_z/d = 4\pi$). We also note that the run time required to obtain adequate statistics does not decrease with domain size. The evolution of large scales takes place in long time scales (cf. § 3.4 for more details), and this strongly affects the value obtained for the mean streamwise velocity.

The effect of the domain size on the results was checked in several ways. First, figure 3(a,b) show the streamwise velocity autocorrelation in the streamwise and spanwise directions. The behaviour of non-rotating Waleffe flow is quite similar to

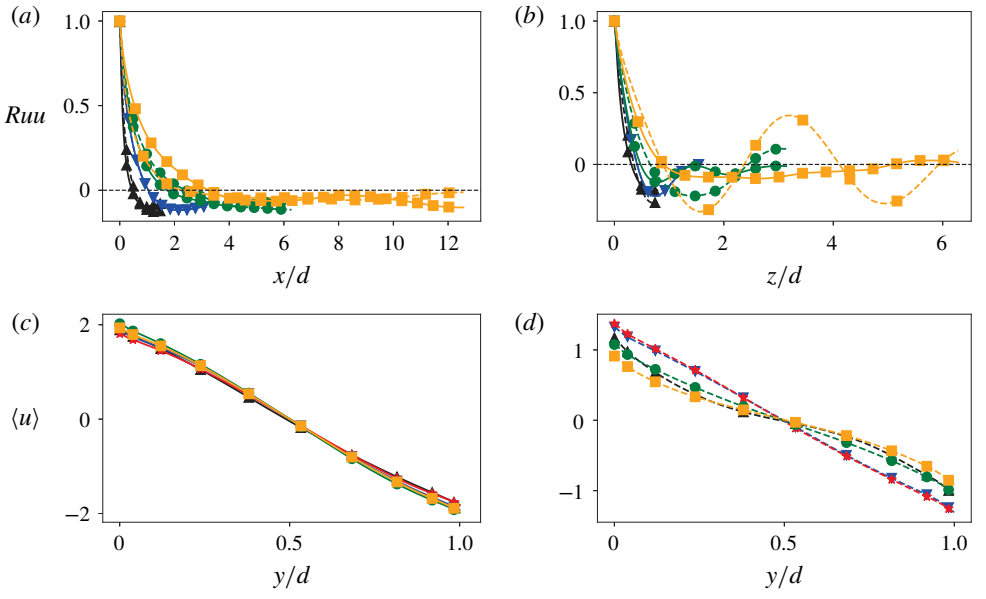

FIGURE 3. (*a*,*b*) The streamwise velocity autocorrelation in the streamwise (*a*) and spanwise (*b*) directions. Solid lines are without rotation ($R_\Omega = 0$) while dashed lines are with mild rotation ($R_\Omega = 0.32$). Symbols: black upward triangle (▲), $L_x/d = \pi$, $L_z/d = \pi/2$; blue downward triangle (▼), $L_x/d = 2\pi$, $L_z/d = \pi$; green circle (●), $L_x/d = 4\pi$, $L_z/d = 2\pi$; and yellow square (■), $L_x/d = 8\pi$, $L_z/d = 4\pi$. (*c*,*d*) The magnitude of averaged streamwise velocity for non-rotating (*c*) and $R_\Omega = 0.32$ (*d*). The three-halves domain (red star (★),$L_x/d = 3\pi$, $L_z/d = \frac{3}{2}\pi$) is also included.

what is commonly seen for plane Couette flow in the streamwise direction, with long decorrelation wavelengths. A strong effect of both rotation and domain size is seen in the autocorrelations, showing that the domain size will affect the behaviour of the structures inside the flow, and that rotation has a crucial effect on large-scale structures. All domains are sufficiently long in both the streamwise and spanwise dimensions for the velocity autocorrelations to change sign at least once. However, the domains are not large enough to show full decorrelation.

Another way to check domain-size independence is done by simply comparing the mean velocities obtained from the different computational domains. Owing to the presence of large-scale structures which fill up the domain, the velocity profiles could be affected by the wavelength of these structures. Doubling the domain would not account for the changing wavelength of these structures, as the domain would simply be filled up with twice as many structures with the same wavelength. To avoid this, we run an additional case with periodicity lengths ($L_x/d = 3\pi$ and $L_z/d = \frac{3}{2}\pi$), denoted as the 'three-halves' domain.

In figure 3(*c*,*d*), we show the streamwise, spanwise and temporally averaged streamwise velocity $\langle u \rangle$ for all cases. Remarkably, for the non-rotating case, the average streamwise velocity for all domains from the smallest domain to the largest collapse on top of each other. For the rotating case, there is collapse between the small and three-halves domain, while the other domains show strong variability.

To understand this variation between the domains, which only appears for the rotating case, we analyse the domain-size effects on the strength of large-scale pinned structures. In figure 4, we show visualizations of the temporally and

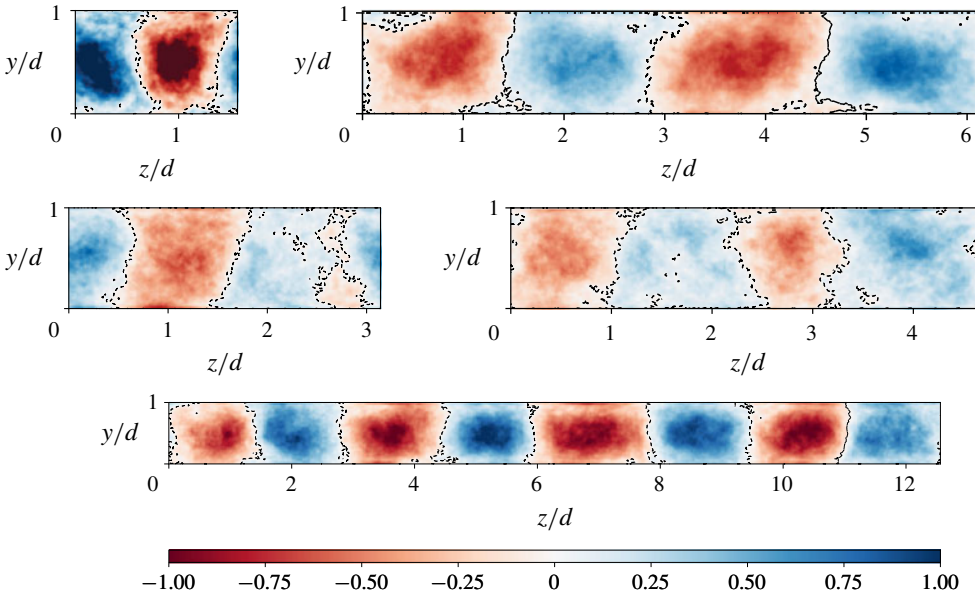

FIGURE 4. Pseudo-colour plot of Ω_x for the five domain sizes simulated, at $R_\Omega = 0.32$. Contours levels for vorticity are shown at zero to highlight the large-scale structures.

streamwise-averaged streamwise vorticity Ω_x. Why this definition of Ω_x captures the large-scale structures is discussed more elaborately in § 3.3, but for now we note that it highlights streamwise-invariant structures that are pinned in the spanwise direction. A strong pinned structure is prominent for the very small domain, due to the constrained periodicity. The structure is somewhat weakened for the small domain, and the colours are less intense on figure 4. The three-halves domain shows an organized pinned structure at three-halves the wavelength of the small domain, which remarkably does not affect the mean flow statistics of figure 3. The medium domain and large domains present a larger number of organized structures, consistent with what is seen in the autocorrelations. Even if the medium and small domains have structures with the same wavenumber, the number of structures is different. This indicates that what is causing the differences in velocities must not be within the structures themselves, but in their interactions with each other and the near-wall regions.

We will not be able to completely remove domain-size effects, as this study shows. From here, we proceed with the 'small' domain with a single structure, as it allows us to explore a large parameter space while running the simulations for long times to gather enough statistics. We acknowledge that domain-size effects are unavoidable.

3. Results

3.1. *The nature of shear transport*

First, we show that the shear force in large-Reynolds-number Waleffe flow is transported almost exclusively by Reynolds stresses. In the statistically stationary regime, the mean velocities do not depend on time. We can write down an average of the total shear τ transported across a wall-normal plane, which is

$$\langle \tau \rangle = \mu \frac{\mathrm{d}\langle u \rangle}{\mathrm{d}y} + \rho \langle uv \rangle, \tag{3.1}$$

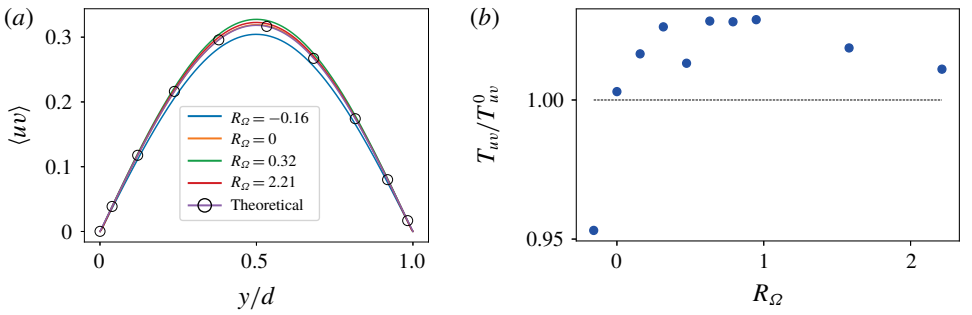

FIGURE 5. (*a*) Averaged transport for different R_Ω values. The theoretical value for fully turbulent shear transport is shown with hollow circles. (*b*) Normalized integrated transport T_{uv} for different R_Ω values.

where ρ is the fluid density and μ is the dynamic viscosity. Equation (3.1) just states that, in the statistically stationary regime, shear is transported either through viscosity or through Reynolds stresses.

In high-Reynolds-number Waleffe flow, we may assume that the viscous shear transport ($\mu\, \mathrm{d}\langle u\rangle/\mathrm{d}y$) is negligible. This is because, as Re increases, the velocity gradients remain approximately constant. No viscous boundary layer where the average velocity has a sharp gradient is formed, because there is no wall with a no-slip condition. Hence, in the turbulent regime, the magnitude of the viscous term in (3.1) is $O(Re^{-1})$ smaller than that of the Reynolds stress term. With this, equation (3.1) becomes

$$\langle \tau \rangle \approx \rho \langle uv \rangle. \tag{3.2}$$

By differentiating (3.1) with respect to the wall-normal direction, and comparing it to the Navier–Stokes equations, we have that the shear transported must be balanced by the body force,

$$\frac{\mathrm{d}\langle \tau \rangle}{\mathrm{d}y} \approx \frac{\mathrm{d}(\rho \langle uv \rangle)}{\mathrm{d}y} \approx \rho \boldsymbol{f}, \tag{3.3}$$

and solving the above equations gives an analytic expression for the Reynolds stress,

$$\langle uv \rangle = \frac{F}{\beta} \sin(\beta y). \tag{3.4}$$

This is valid in the statistically stationary regime only if our assumption that shear transport is fully due to Reynolds stresses. We check this in figure 5(*a*), where we show the $\langle uv \rangle$ Reynolds stress components for different rotation numbers, as well as the theoretical value for $\langle uv \rangle$ from (3.4). We find that $\langle uv \rangle$ is almost equal to the theoretical value for full shear transport due to Reynolds stresses for all rotation numbers shown, even if some deviations exist for $R_\Omega = -0.16$, i.e. cyclonic rotation.

To further quantify transport, we define T_{uv} as the integrated momentum transport in the wall-normal direction,

$$T_{uv} = \int_0^d \langle uv \rangle \, \mathrm{d}y, \tag{3.5}$$

and calculate its deviation from the analytical value for purely turbulent transport $T^o_{uv} = 2F/\beta^2 \approx 0.202Fd^2$. We show this quantity in figure 5(*b*). The numerical values

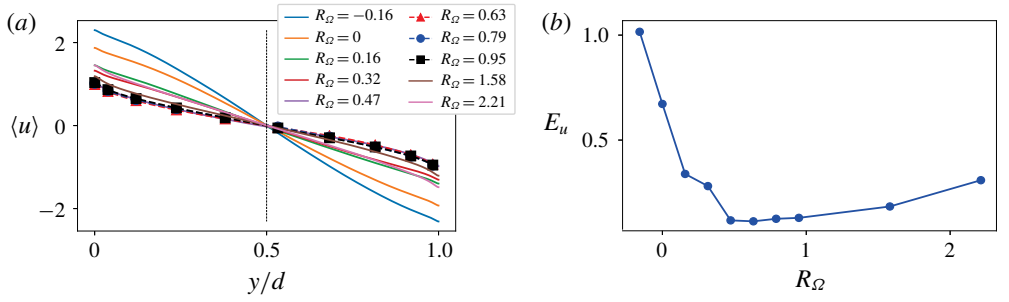

FIGURE 6. (*a*) Averaged streamwise velocity $\langle u \rangle$ for different values of R_Ω. (*b*) Average kinetic energy of the mean streamwise flow E_u for different values of R_Ω.

of T_{uv} are within approximately 3 % of the theoretical value for different rotation numbers, except for $R_\Omega = -0.16$, corresponding to the case with cyclonic rotation. This tells us two things. First, that, as seen in plane Couette and Taylor–Couette flow, cyclonic rotation hampers turbulence and, in this case, the viscous transport accounts for ∼5 % of the total transport. Second, that, for no rotation or anticyclonic rotation, the shear transport is fully turbulent and T_{uv} instead gives us an estimate for the temporal convergence errors in the simulations, as T_{uv}/T^o_{uv} is close to unity. From figure 5(*b*), these can be estimated at approximately 2 %–3 %.

Unlike previous studies of rotating plane Couette flow (Brauckmann *et al.* 2016), where the transported shear was a response of the system, an optimum momentum transport cannot be deduced from T_{uv}, because this is an input of the simulation, and $T_{uv} \approx T^o_{uv}$ in all cases. To define an optimum momentum transport, we must turn towards other diagnostics. This is further investigated in §§ 3.2 and 3.3.

3.2. *Velocity magnitudes and optimum shear transport*

We now analyse the effect of rotation on the velocity profiles. In figure 6(*a*), we show the averaged streamwise velocity profiles between the free-slip walls for various rotation numbers R_Ω. First, it can be seen that the velocity profiles are symmetric around the mid-gap ($y/d = 0.5$), and that the slip velocity at the walls is maximum for $R_\Omega = -0.16$. As the rotation number increases, the velocity profiles show a decrease in the slip velocity until a minimum is reached at approximately $R_\Omega = 0.63$.

To quantify this, we define E_u, the average streamwise kinetic energy of the flow, as

$$E_u = \frac{1}{2d}\int_0^d \langle u \rangle^2 \, \mathrm{d}y = \frac{1}{2}U^{*2}, \tag{3.6}$$

with U^* a characteristic streamwise mean velocity. This U^* is a response of the system. The dependence of E_u on R_Ω is shown in figure 6(*b*). As anticyclonic rotation is introduced, a prominent decrease of E_u is seen, with a flat plateau around $R_\Omega = 0.4$–1.5, after which E_u increases again. This means that the same amount of momentum T_{uv} (response) is transferred with a smaller velocity (input). We can use this to define the optimum shear transport as the value of R_Ω for which E_u is minimum. With this interpretation, we can say that, for our simulations of rotating Waleffe flow, optimal transport appears as a broad 'peak' (which is actually a minimum) in a large range of R_Ω, similar to what was observed in low-Reynolds-number plane Couette flow by Brauckmann *et al.* (2016). The minimum

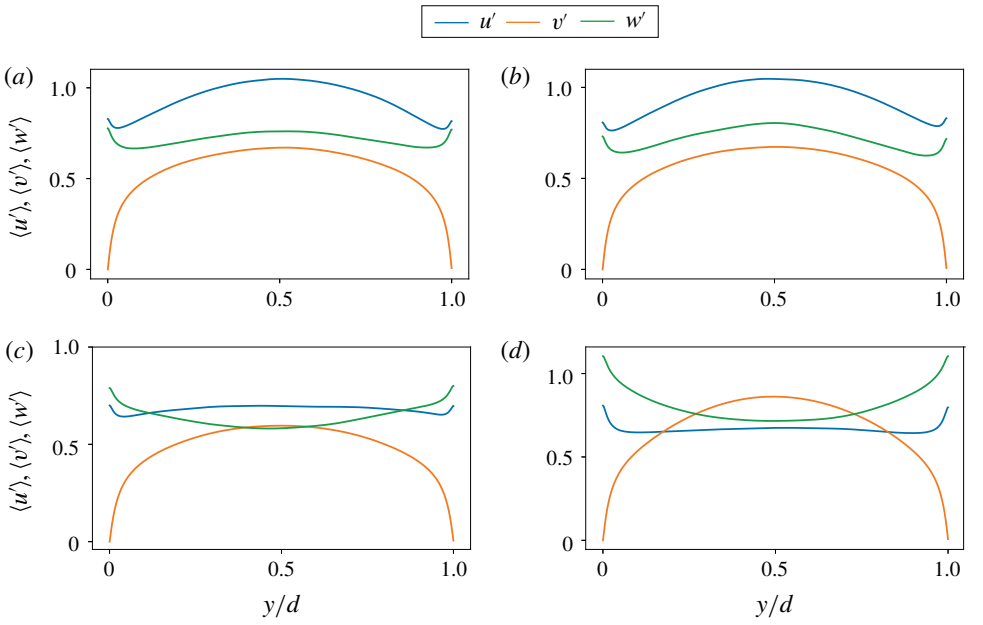

FIGURE 7. Root-mean-square velocity fluctuations at $R_\Omega = -0.16$ (*a*), $R_\Omega = 0$ (*b*), $R_\Omega = 0.63$ (*c*) and $R_\Omega = 2.21$ (*d*).

E_u is located at approximately $R_\Omega \approx 0.63$, but that minimum lies on a relatively smooth valley in the range $R_\Omega \in (0.4, 1.0)$.

To understand the mechanisms behind the optimal transport, we turn to the velocity root-mean-square velocity fluctuation profiles, shown in figure 7 for some selected values of R_Ω. The first thing we notice is the absence of a near-wall peak in the streamwise velocity fluctuation profiles. Instead, a local minimum is seen in some, but not all, cases. This suggests the absence of ordinary boundary layers due to the stress-free boundary condition. We expect that the high-Reynolds-number boundary layer instability behind the narrow peak optimum transport in plane Couette flow (Brauckmann & Eckhardt 2017) will be absent.

The second thing we notice is that, for cyclonic and no rotation, the streamwise velocity fluctuations $\langle u' \rangle$ are largest of the three components at the mid-gap, but, as R_Ω increases, the largest fluctuations become the ones in the wall-normal direction ($\langle v' \rangle$). The largest streamwise velocity fluctuations $\langle u' \rangle$ appear when $R_\Omega = -0.16$, i.e. R_Ω is minimum. As R_Ω is increased, the values of $\langle u' \rangle$ monotonically decrease. The smallest value of fluctuations corresponds to the largest value of $R_\Omega = 2.21$. However, for the wall-normal velocity fluctuations, the opposite pattern is seen, and the values of $\langle v' \rangle$ increase with increasing R_Ω up to $R_\Omega = 2.21$. The spanwise fluctuations show no discernible pattern in their variation with R_Ω. This gives a hint to the mechanism behind optimum transport: the Coriolis forces due to spanwise rotation appear with different signs in the streamwise (x) and wall-normal (y) components of the Navier–Stokes equations, in one case increasing the fluctuations, in the other decreasing them.

3.3. *The effect of rotation on large-scale structures*

We now turn to the effect of rotation on large-scale structures. A visualization of the instantaneous streamwise velocity is shown in figure 8, with instantaneous

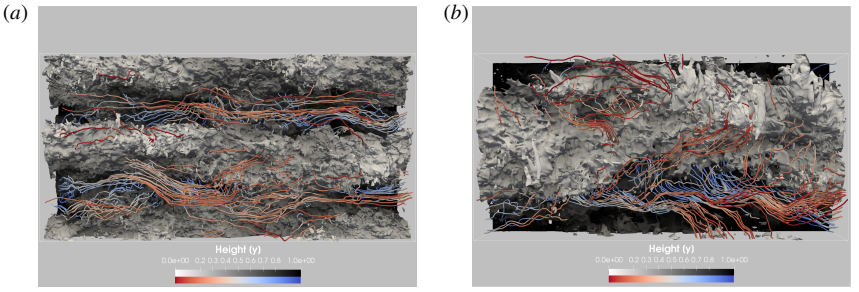

FIGURE 8. Contour of instantaneous streamwise velocity u at $R_\Omega = 0.0$ (a), contour at $u = 0.15$, and $R_\Omega = 0.63$ (b), contour at $u = -0.1$. The view is projected onto a x–z plane, with the y coordinate represented through colour. Flow is from left to right. The instantaneous streamlines are added, and coloured according to y coordinate.

streamlines superimposed. We first observe the presence of large-scale structures in the flow for both the rotating and non-rotating cases. This could be expected from the autocorrelations in figure 3.

Large-scale flows can be considered secondary flows if their velocity components are perpendicular to the main flow direction. This is not always the case. In the absence of rotation, the streamwise velocity contour in figure 8 is largely invariant in the streamwise direction. The secondary flow, i.e. the cross-flow in the wall-normal and spanwise directions, is very weak. This can be deduced from the relatively straight path of the streamlines. From this, we do not expect it to play a role in transporting shear.

As anticyclonic rotation is introduced, the flow is heavily modified. The streamwise velocity contour now has a completely different shape. More importantly, the secondary flow is strengthened, as can be seen from the visualized streamlines, which move more in the wall-normal and spanwise direction. This secondary flow is of crucial importance, as it helps with the transport of shear.

To analyse these structures more quantitatively, we proceed in an analogous manner to Sacco *et al.* (2019). Secondary flows are captured through the streamwise vorticity, as they are perpendicular to the main flow direction. By looking at the streamwise and temporal average of this quantity (Ω_x), we capture only the spanwise-pinned streamwise-invariant structures, which are known to be the most relevant for shear transport. If large-scale structures are moving around the computational domain, they would not be captured by Ω_x, as the averages would vanish.

Figure 9 shows Ω_x for different values of R_Ω. As hinted at by figure 8, spanwise-pinned and streamwise-invariant secondary flows, with a vorticity core, appear as anticyclonic rotation is introduced. The strength of the roll-like structures appears to increase with increasing anticyclonic rotation. At approximately $R_\Omega \approx 1.5$, the trend changes, and further increasing the rotation makes the structures unorganized, as shown in figure 9(d) at $R_\Omega = 2.21$.

To quantify the strength of the rolls, we define the mean-squared circulation of the rolls as the volume integral

$$\Gamma_2 = \frac{1}{dL_z} \int_0^d \int_0^{L_z} \Omega_x^2 \, \mathrm{d}y \, \mathrm{d}z, \tag{3.7}$$

and show this as a function of R_Ω in figure 9(e). We can see how the strength of the pinned rolls increases with increasing R_Ω until the maximum is reached. However,

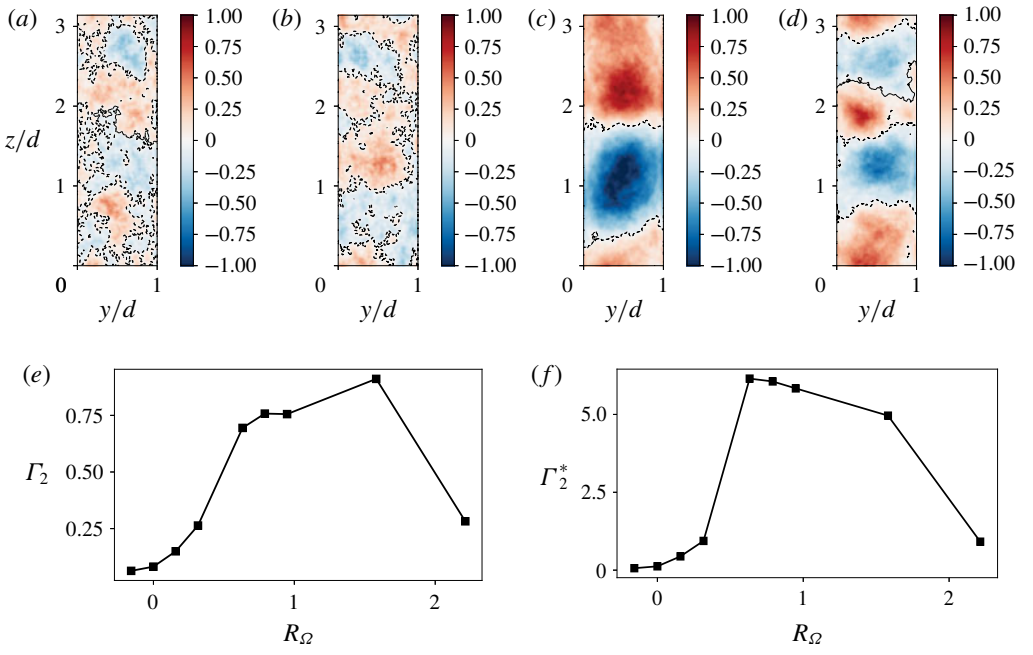

FIGURE 9. Panels (*a–d*) represent the streamwise and temporally averaged streamwise vorticity Ω_x for $R_\Omega = -0.16$, 0.0, 0.63 and 2.21 (left to right). A black contour at zero has been added to delineate negative vorticity from positive vorticity regions. Panel (*e*) shows the averaged circulation energy Γ_2 for the large-scale structures in the range of $R_\Omega \in [-0.16, 2.21]$, and panel (*f*) depicts the effective averaged circulation energy Γ_2^* in the same R_Ω range.

using R_Ω to compare roll strength is not totally fair. As shown in § 3.2, the underlying magnitudes of velocity change. Therefore, we define $\Gamma_2^* = \Gamma_2 \tilde{U}^2/U^{*2}$, where U^*, a characteristic streamwise velocity, was defined in (3.6). We show Γ_2^* as a function of R_Ω in figure 9(*f*), and observe that the strongest and most ordered structures correspond to the range $R_\Omega = 0.47$–1. This coincides with the range of R_Ω for which optimal shear transport takes place, and highlights the link between optimal transport and strongest large-scale structures as was seen in plane Couette flow by Brauckmann & Eckhardt (2013, 2017).

3.4. *Large-scale structures and the self-sustained process*

First, we visually compare the rolls in rotating Waleffe flow to those in rotating plane Couette flow in figure 10 using Ω_x. One thing we notice is that these structures are more clearly defined in plane Couette flow than in Waleffe flow. Furthermore, the streamwise vorticity of the rolls is localized in the core of the structures in Waleffe flow. The streamwise vorticity in plane Couette flow is localized mainly in the boundaries of the structure, with additional vorticity being generated by the boundary layers. Nevertheless, these results show that pinned large-scale structures arise only with a generic shear and anticyclonic rotation.

We can probe the temporal behaviour of the large-scale structure. In Sacco *et al.* (2019), a link between the large-scale fixed structures in Taylor–Couette flow, i.e. the

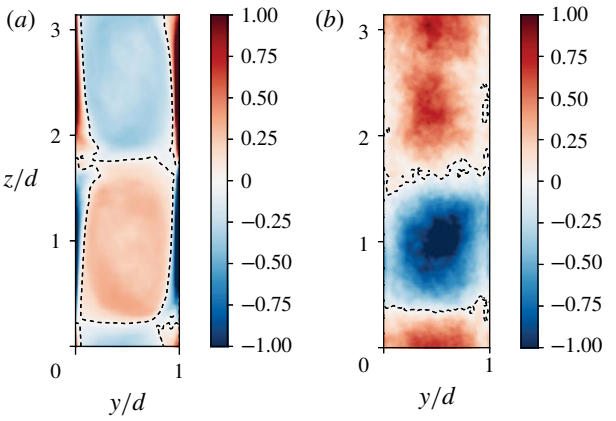

FIGURE 10. Pseudo-colour plot of temporally averaged streamwise vorticity Ω_x for plane Couette flow at $R_\Omega = 0.1$ (*a*) and rotating Waleffe flow at $R_\Omega = 0.63$ (*b*). Contour levels for vorticity are shown at zero to highlight the large-scale structures.

turbulent Taylor rolls, and the SSP was found by analysing the rolls in Fourier space following Hamilton *et al.* (1995). While the analogy was far from perfect, the mean flow energy was found to oscillate in antiphase with the spanwise fundamental mode, which represented the large-scale structure through its rolls and streaks.

We proceed in the same manner, and we begin by defining the modal root-mean-square velocity as

$$M(k_x = \alpha m, k_z = \beta n) = \left[\int_0^d (\hat{u}^2(m\alpha, y, n\beta) + \hat{v}^2(m\alpha, y, n\beta) + \hat{w}^2(m\alpha, y, n\beta))\, \mathrm{d}y \right]^{1/2}, \tag{3.8}$$

where $\alpha = 2\pi/L_x$ and $\beta = 2\pi/L_z$ are the fundamental streamwise and spanwise wavenumbers, and $\hat{\phi}$ represents the Fourier transform of ϕ in the spanwise and streamwise directions. We focus on two modes: $M(0,\ 0)$, the spanwise- and streamwise-invariant mode, which represents the mean flow; and $M(0,\ \beta)$, the streamwise-independent fundamental in z, corresponding to the large-scale structure.

In figure 11 we see that the energies of these two modes oscillate on time scales of $O(50d/\tilde{U})$, and the period of the two quantities is almost anticorrelated, consistent with the breakdown–regeneration structure of shear flows described in Hamilton *et al.* (1995), and the behaviour of the turbulent Taylor rolls in Sacco *et al.* (2019). Energy is constantly being redistributed from the mean flow into the streaks and rolls of the large-scale structure. Remarkably, there are some 'dead' times ($t\tilde{U}/d = 200$–300) where the cycle is temporarily broken and there is no significant exchange of energy.

We can probe the origin of the structures following the procedure set out in Pirozzoli *et al.* (2018). Secondary flows are perpendicular to the main flow, and as such will have vorticity mainly in the main flow direction, i.e. the streamwise direction. Starting off with a Reynolds-averaged (in the streamwise and time coordinates) equation for Ω_x (Einstein & Li 1958), we have

$$\overline{v}\frac{\partial \Omega_x}{\partial y} + \overline{w}\frac{\partial \Omega_x}{\partial z} = \left(\frac{\partial^2}{\partial y^2} - \frac{\partial^2}{\partial z^2}\right)(-\langle \overline{v'w'} \rangle) + \frac{\partial^2}{\partial y \partial z}(\overline{v'^2} - \overline{w'^2}) + \nu\left(\frac{\partial^2 \Omega_x}{\partial z^2} + \frac{\partial^2 \Omega_x}{\partial z^2}\right), \tag{3.9}$$

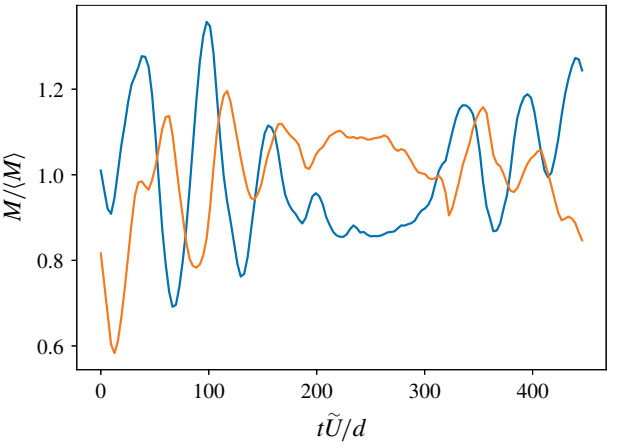

FIGURE 11. Temporal evolution of the normalized modal root-mean-square velocity in the Fourier space associated with the $M(0, \beta)$ mode (orange) and the $M(0, 0)$ mode (blue) for $R_\Omega = 0.63$.

where $\overline{\phi}$ denotes a temporal and streamwise average, ϕ' are fluctuations around that mean and $\overline{\omega}_x$ is simply Ω_x. The various terms in this equation are associated with the effect of mean cross-stream convection (left-hand side), secondary turbulent shear stress (first term on right-hand side), normal stress anisotropy (second term) and viscous diffusion (third term). If the convective terms vanish, the convective transport of average streamwise vorticity is zero. If this holds, it should be possible to write a streamfunction for the cross-flow secondary motions which has a strict functional relationship to the vorticity (Pirozzoli *et al.* 2018).

The streamfunction is evaluated by solving

$$\nabla^2\psi = -\Omega_x, \tag{3.10}$$

with a constant Dirichlet boundary conditions at the walls, because the stress-free walls behave like a streamline. We take this free constant to be zero.

In figure 12(*a*,*b*), we superimpose contours of constant ψ onto a pseudo-colour plot of Ω_x. No clear relationship can be seen for $R_\Omega = 0$, but the circular contours of ψ at $R_\Omega = 0.63$ overlap onto the large-scale structures of Ω_x, making evident the relationship between ψ and Ω_x. The functional relationship between ψ and Ω_x is shown more prominently in figure 12(*d*), where a scatterplot of ψ and Ω_x for $0.1 < y/d < 0.9$ is shown. A quasi-linear relationship between them can be seen in the regions far away from the wall.

This can be understood following Pirozzoli *et al.* (2018), who decomposed Ω_x as eigenfunctions of the Laplace operator:

$$(\nabla^2 + k^2)\psi = 0. \tag{3.11}$$

The admissible values of k give us the different eigenfunctions of the Laplacian. A linear regression, fitted to data at $y/d \in [0.1, 0.9]$, shows the best-fitting line coefficient (k^2) at 6.96×10^{-2}, giving the value of $\Omega_x = k^2\psi$. This indicates that the fixed secondary motions in Waleffe flow correspond very well to a single eigenmode of the Laplacian operator. Overall, these results differ little from those obtained in plane Couette flow, showing that the behaviour of the large scales is barely affected by the no-slip condition.

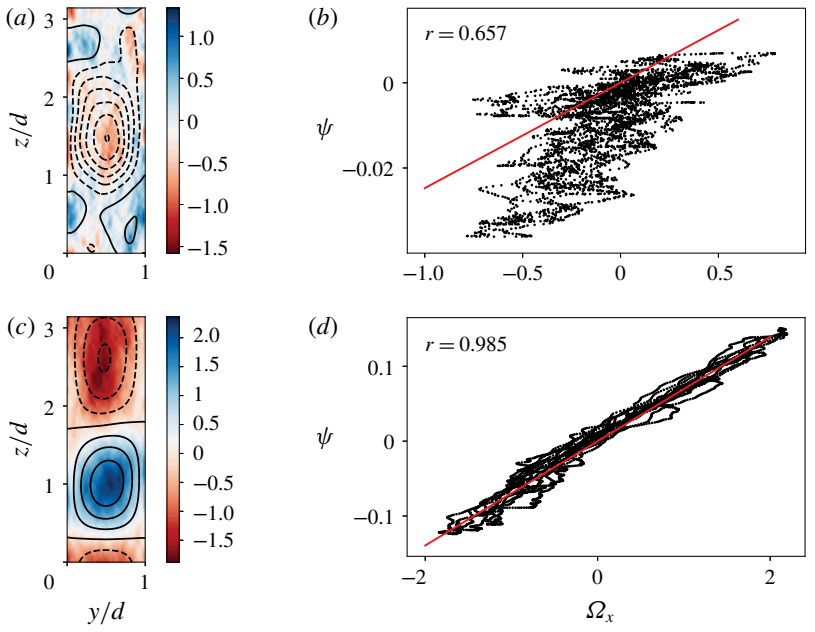

FIGURE 12. (*a*,*c*) Pseudo-colour plot showing Ω_x at $R_\Omega = 0$ (*a*,*b*) and $R_\Omega = 0.63$ (*c*,*d*) with contours of constant ψ superimposed. The contours on the plot in (*a*) are spaced 0.012 units of ψ, while on the plot in (*b*) they are spaced 0.04 units of ψ, with dashed contours indicating negative values of ψ. (*b*,*d*) Scatterplots of ψ against Ω_x corresponding to the plots on the left. The best linear fit is plotted in red.

4. Summary and conclusions

We performed DNS of rotating Waleffe flow at a fixed $Re = 3.61 \times 10^3$. Once adequate resolution was determined, a study of the effect of domain size was performed. The decorrelation lengths in the spanwise and streamwise directions were shown to have a strong dependence on the domain size. They further revealed that rotation does not substantially affect the velocity autocorrelations in the streamwise direction, but that it has a strong effect on the spanwise direction, as it modifies the large-scale structures.

Anticyclonic spanwise rotation modifies the shear transport, and an 'optimal' shear transport appears at approximately $R_\Omega \approx 0.63$, inasmuch as the mean streamwise energy is reduced to a minimum for a fixed shear transport. This is because the transported shear has to equal the underlying forcing. Anticyclonic rotation also modifies the underlying velocity fluctuation profiles, heavily decreasing streamwise fluctuations and enhancing wall-normal fluctuations.

Owing to the absence of boundary layers, we linked optimal transport in rotating Waleffe flow to the broad peak of optimal shear transport in plane Couette flow found by Brauckmann *et al.* (2016). In a similar manner as discussed in Brauckmann & Eckhardt (2013) and Brauckmann *et al.* (2016), this 'peak' is linked to the appearance and strengthening of pinned large-scale structures. Once the energy was corrected to account for the varying strength of the mean flow, these structures were found to be strongest at approximately the same values of $R_\Omega \in (0.4, 1)$, which corresponds to the value of R_Ω that achieves optimal transport. The structures were found to periodically

take energy from the mean flow to energize, and were also linked to eigenvalues of a streamfunction for secondary flows, following Pirozzoli *et al.* (2018).

With these simulations we have shown that the appearance of streamwise-invariant, spanwise-pinned structures that increase transport are a generic characteristic of anticyclonic shear flows, appearing in both rotating Waleffe and rotating plane Couette flows. We note that these structures appear to be invariant in a direction normal to rotation, unlike those which could be expected from the Taylor–Proudman problem. An avenue for further research, aside from increasing the Reynolds number, is probing homogeneous shear turbulence to search for these structures. This system removes the last confinement on the structures, the no-penetration top and bottom walls.

Acknowledgements

We thank B. Eckhardt, S. Pirozzolli, F. Sacco and R. Verzicco for fruitful discussions. We thank the Center for Advanced Computing and Data Science (CACDS) at the University of Houston for providing computing resources.

REFERENCES

ANDERECK, C. D., LIU, S. S. & SWINNEY, H. L. 1986 Flow regimes in a circular Couette system with independently rotating cylinders. *J. Fluid Mech.* **164**, 155–183.

BEAUME, C., CHINI, G. P., JULIEN, K. & KNOBLOCH, E. 2015 Reduced description of exact coherent states in parallel shear flows. *Phys. Rev.* E **91** (4), 043010.

BRAUCKMANN, H. J. & ECKHARDT, B. 2013 Intermittent boundary layers and torque maxima in Taylor–Couette flow. *Phys. Rev.* E **87**, 033004.

BRAUCKMANN, H. J. & ECKHARDT, B. 2017 Marginally stable and turbulent boundary layers in low-curvature Taylor–Couette flow. *J. Fluid Mech.* **815**, 149–168.

BRAUCKMANN, H. J., SALEWSKI, M. & ECKHARDT, B. 2016 Momentum transport in Taylor–Couette flow with vanishing curvature. *J. Fluid Mech.* **790**.

CHANTRY, M., TUCKERMAN, L. S. & BARKLEY, D. 2016 Turbulent–laminar patterns in shear flows without walls. *J. Fluid Mech.* **791**, R8.

DESSUP, T., TUCKERMAN, L. S., WESFREID, J. E., BARKLEY, D. & WILLIS, A. P. 2018 The self-sustaining process in Taylor–Couette flow. *Phys. Rev. Fluids* **3** (12), 123902.

DRAZIN, P. G. & REID, W. H. 2004 *Hydrodynamic Stability*. Cambridge University Press.

ECKHARDT, B., SCHNEIDER, T. M., HÖF, B. & WESTERWEEL, J. 2007 Turbulence transition in pipe flow. *Annu. Rev. Fluid Mech.* **39**, 447.

EINSTEIN, H. A. & LI, H. 1958 Secondary currents in straight channels. *EOS Trans. AGU* **39** (6), 1085–1088.

VAN GILS, D. P. M., HUISMAN, S. G., GROSSMANN, S., SUN, C. & LOHSE, D. 2012 Optimal Taylor–Couette turbulence. *J. Fluid Mech.* **706**, 118–149.

GROSSMANN, S., LOHSE, D. & SUN, C. 2016 High-Reynolds number Taylor–Couette turbulence. *Annu. Rev. Fluid Mech.* **48**, 53–80.

HAMILTON, J. M., KIM, J. & WALEFFE, F. 1995 Regeneration mechanisms of near-wall turbulence structures. *J. Fluid Mech.* **287**, 317–348.

HUISMAN, S. G., VAN DER VEEN, R. C. A., SUN, C. & LOHSE, D. 2014 Multiple states in highly turbulent Taylor–Couette flow. *Nature Comm.* **5**, 3820.

JIMENEZ, J. 2012 Cascades in wall-bounded turbulence. *Annu. Rev. Fluid. Mech.* **44**, 27–45.

KIM, J., MOIN, P. & MOSER, R. 1987 Turbulence statistics in fully developed channel flow at low Reynolds number. *J. Fluid Mech.* **177**, 133–166.

LATHROP, D. P., FINEBERG, J. & SWINNEY, H. L. 1992 Turbulent flow between concentric rotating cylinders at large Reynolds number. *Phys. Rev. Fluids* **68** (10), 1515–1518.

LEE, M. & MOSER, R. D. 2015 Direct numerical simulation of turbulent channel flow up to $Re_\tau \approx 5200$. *J. Fluid Mech.* **774**, 395–415.

MOIN, P. & KIM, J. 1982 Numerical investigation of turbulent channel flow. *J. Fluid Mech.* **118**, 341–377.

MOSER, R. D. & MOIN, P. 1984 Direct numerical simulation of curved turbulent channel flow. NASA TM 8597.

OSTILLA-MÓNICO, R., VAN DER POEL, E. P., VERZICCO, R., GROSSMANN, S. & LOHSE, D. 2014 Exploring the phase diagram of fully turbulent Taylor–Couette flow. *J. Fluid Mech.* **761**, 1–26.

PIROZZOLI, S., MODESTI, D., ORLANDI, P. & GRASSO, F. 2018 Turbulence and secondary motions in square duct flow. *J. Fluid Mech.* **840**, 631–655.

VAN DER POEL, E. P., OSTILLA-MÓNICO, R., DONNERS, J. & VERZICCO, R. 2015 A pencil distributed finite difference code for strongly turbulent wall-bounded flows. *Comput. Fluids* **116**, 10–16.

RAVELET, F., MARIÉ, L., CHIFFAUDEL, A. & DAVIAUD, F. 2004 Multistability and memory effect in a highly turbulent flow: experimental evidence for a global bifurcation. *Phys. Rev. Lett.* **93**, 164501.

SACCO, F., VERZICCO, R. & OSTILLA-MÓNICO, R. 2019 Dynamics and evolution of turbulent Taylor rolls. *J. Fluid Mech.* **870**, 970–987.

SMITS, A. J., MCKEON, B. J. & MARUSIC, I. 2011 High-Reynolds number wall turbulence. *Annu. Rev. Fluid. Mech.* **43**, 353–375.

TAYLOR, G. I. 1923 Stability of a viscous liquid contained between two rotating cylinders. *Phil. Trans. R. Soc. Lond.* A **223**, 289–343.

TOLLMIEN, W. 1936 General instability criterion of laminar velocity distributions. NACA TM 792.

VERZICCO, R. & ORLANDI, P. 1996 A finite-difference scheme for three-dimensional incompressible flow in cylindrical coordinates. *J. Comput. Phys.* **123**, 402–413.

WALEFFE, F. 1997 On a self-sustaining process in shear flows. *Phys. Fluids* **9**, 883–900.

ZANDBERGEN, P. J. & DIJKSTRA, D. 1987 Von Kármán swirling flows. *Annu. Rev. Fluid Mech.* **19** (1), 465–491.